Journal of ELECTRONIC MATERIALS, Vol. 47, No. 9, 2018
https://doi.org/10.1007/s11664-018-6214-9

TOPICAL COLLECTION: 17TH CONFERENCE ON DEFECTS (DRIP XVII)

Defect Characterization, Imaging, and Control in Wide-Bandgap Semiconductors and Devices

L.J. BRILLSON,[1,2,6] G.M. FOSTER,[2] J. COX,[1] W.T. RUANE,[2] A.B. JARJOUR,[2] H. GAO,[2] H. VON WENCKSTERN,[3] M. GRUNDMANN,[3] B. WANG,[4] D.C. LOOK,[4] A. HYLAND,[5] and M.W. ALLEN[5]

1.—Department of Electrical and Computer Engineering, The Ohio State University, Columbus, OH 43210, USA. 2.—Department of Physics, The Ohio State University, Columbus, OH 43210, USA. 3.—Institute for Experimental Physics, University of Leipzig, Postfach 10 09, 04103 Leipzig, Germany. 4.—Semiconductor Research Center, Wright State University, Dayton, OH 45435, USA. 5.—Department of Electrical and Computer Engineering, University of Canterbury, Christchurch 8140, New Zealand. 6.—e-mail: brillson.1@osu.edu

Wide-bandgap semiconductors are now leading the way to new physical phenomena and device applications at nanoscale dimensions. The impact of defects on the electronic properties of these materials increases as their size decreases, motivating new techniques to characterize and begin to control these electronic states. Leading these advances have been the semiconductors ZnO, GaN, and related materials. This paper highlights the importance of native point defects in these semiconductors and describes how a complement of spatially localized surface science and spectroscopy techniques in three dimensions can characterize, image, and begin to control these electronic states at the nanoscale. A combination of characterization techniques including depth-resolved cathodoluminescence spectroscopy, surface photovoltage spectroscopy, and hyperspectral imaging can describe the nature and distribution of defects at interfaces at both bulk and nanoscale surfaces, their metal interfaces, and inside nanostructures themselves. These features as well as temperature and mechanical strain inside wide-bandgap device structures at the nanoscale can be measured even while these devices are operating. These advanced capabilities enable several new directions for describing defects at the nanoscale, showing how they contribute to device degradation, and guiding growth processes to control them.

Key words: Wide-bandgap semiconductor, defect, cathodoluminescence spectroscopy, surface photovoltage spectroscopy, hyperspectral imaging, ZnO, GaN, AlGaN, SiC, nanowire, high-electron-mobility transistor

INTRODUCTION

Wide-bandgap semiconductors are now at the forefront of solid-state electronics. These materials are envisioned for a wide array of advanced electronic structures such as: (1) transparent conducting oxides (TCOs)[1,2] for solar cells, biosensors, and wearable electronics, (2) high-mobility two-dimensional electron gas (2DEG) heterojunctions[3,4] for interface superconductivity, magnetism, and multiferroicity, (3) high-frequency communication packages with low dielectric loss for voltage-tunable filters, oscillators, and phase shifters, and (4) low-leakage, high-breakdown-voltage structures for tunnel junctions, high-k dielectric capacitors, and high-power transistors.[5,6] Native point defects impact these applications strongly by introducing recombination and scattering centers that reduce mobility,

(Received November 22, 2017; accepted March 7, 2018; published online March 19, 2018)

carrier and spin transport, optical emission, voltage control, and device reliability.

Depth-resolved cathodoluminescence spectroscopy (DRCLS)[7] combined with surface photovoltage spectroscopy (SPS),[8] and hyperspectral imaging (HSI) can describe the nature and spatial distribution of native point defects in bulk semiconductors, their microstructures, and their interfaces extending down to the nanoscale. With these optical and electronic techniques, it is possible to characterize the impact of these defects on actual device structures, even while they are operating, in order to gauge temperature and strain as well as how they can introduce new defects that degrade device performance. In turn, these characterization techniques can guide methods to reduce defects and improve electronic properties.

EXPERIMENTAL PROCEDURES

The DRCLS technique[9] involves an incident electron beam that generates a cascade of secondary electrons. At keV energies, electrons lose energy first by generating x-rays, then plasmons, and finally via impact ionization, which generates electron-hole (e-h) pairs that can recombine across the semiconductor bandgap or between band edges and states within the bandgap.[10] The intensities of these gap-state features relative to the bulk band transitions provides a gauge of defect density which can be calibrated using other techniques such as Hall-effect measurements, positron annihilation spectroscopy (PAS), deep-level optical spectroscopy (DLOS), and transient surface photovoltage spectroscopy (t-SPS). Use of scanning electron microscopy (SEM) provides nanoscale spatial resolution both depthwise and laterally. With HSI, i.e., single-wavelength intensity maps extracted from full spectra acquired pixel by pixel across extended areas,[11] one can "map" the spatial distribution of defect luminescence laterally in two dimensions.[12,13] Our DRCLS chambers' ultrahigh-vacuum (UHV) environment enables electron beam energies as low as 0.1 keV to provide near-nanometer depth resolution by avoiding nonradiative e-h recombination due to surface carbon deposited from beam-dissociated CO_2.

RESULTS AND DISCUSSION

The lateral resolution of the DRCLS beam provides useful information about Schottky barrier formation at metal interfaces with wide-bandgap semiconductors; For example, Fig. 1a illustrates DRCL spectra taken from ZnO, both through an Au diode overlayer as well as at the bare ZnO periphery.[14] Spectral features include the near-band-edge (NBE) conduction-to-valence band emission, longitudinal optical (LO) phonon replicas spaced at 73 meV multiples below the NBE peak, and a broad feature at 2.5 eV attributed to an oxygen-vacancy-related (V_O-R) defect in the ZnO. For more reactive metals such as Al or Ta, comparison of metallized versus bare surface spectra reveals metal-induced differences due to formation of near-interface defects.[15] The depth resolution of DRCLS enables one to probe the intimate metal-semiconductor interface, where diffusion and chemical reaction can produce defects.

The lateral resolution of DRCLS permits measurements of electronic inhomogeneity within individual metal diodes; For example, Ni diodes on 4H-SiC exhibit pronounced differences in deep-level defect emissions within the same 500-μm-diameter diode.[16,17] This diode exhibited two deep-level defect emissions, one which varied laterally inside the diode. As with similar diodes on the same surface, current-voltage (I-V) measurements exhibited "double-diode" behavior with kinks that exhibited two distinct Schottky barrier heights. The Fermi level E_F positions within the SiC bandgap corresponding to these Schottky barriers corresponded closely to the optical transition energies between the energy levels of the observed defects and the valence band. These results demonstrated that the deep-level defects observed at the nanoscale produced E_F "pinning" that determined the macroscopic Schottky barrier I-V characteristics, regardless of the metal overlayer's properties.

Native point defects can not only be localized laterally and at interfaces of wide-bandgap semiconductors, but they may also distribute in three dimensions inside nanostructures. Figure 1b illustrates an array of 300-nm- to 500-nm-diameter ZnO nanotripods. Figure 1c shows the HSI map of 2.5-eV V_O-related defects inside individual ZnO nanowires. There is a high V_O-R intensity at the free surfaces of the nanowires and a gradual decrease in defect intensity from surface to bulk over a thickness range of 50 nm to 100 nm. These images show that native point defects are inside as well as on the surface of nanostructures.

Three-dimensional modeling of the DRCLS process can take into account the spatial distribution of the electron cascade's energy loss, the distribution of defects, and the refraction of cathodoluminescence emitted from inside the nanostructure.[18] Figure 2a illustrates schematically the electron cascade positioned with respect to a specific distribution of defects inside a ZnO nanowire. Figure 2b shows defect intensities versus position in a profile measured transverse to the nanowire length, compared with trial defect distributions. These show that V_O-related defects extend hundreds of nanometers away from a free ZnO surface. Other ZnO nano- and microwires display different native point defects that depend on the method of growth.[19] Thus, pulsed laser deposition (PLD) can exhibit features due to Cu_{Zn} substitutional impurities, due to Cu impurities in the Zn source material. Chemical vapor deposition (CVD) can yield V_O-R features as in Fig. 1a, whereas degenerately Ga-doped ZnO exhibits Zn vacancies V_{Zn}. These defect differences

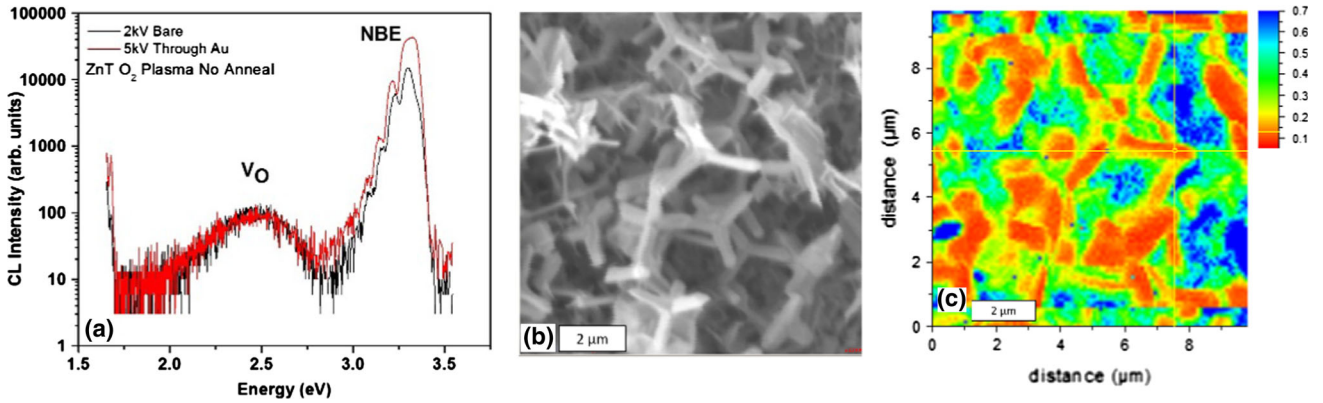

Fig. 1. (a) DRCL spectra of 5-kV electrons through an Au diode layer on ZnO and a 2-kV beam at the diode periphery. Both show dominant 2.5-eV defect emission. (b) SEM micrograph of a ZnO tetrapod array. (c) Corresponding 2.5-eV HSI map.

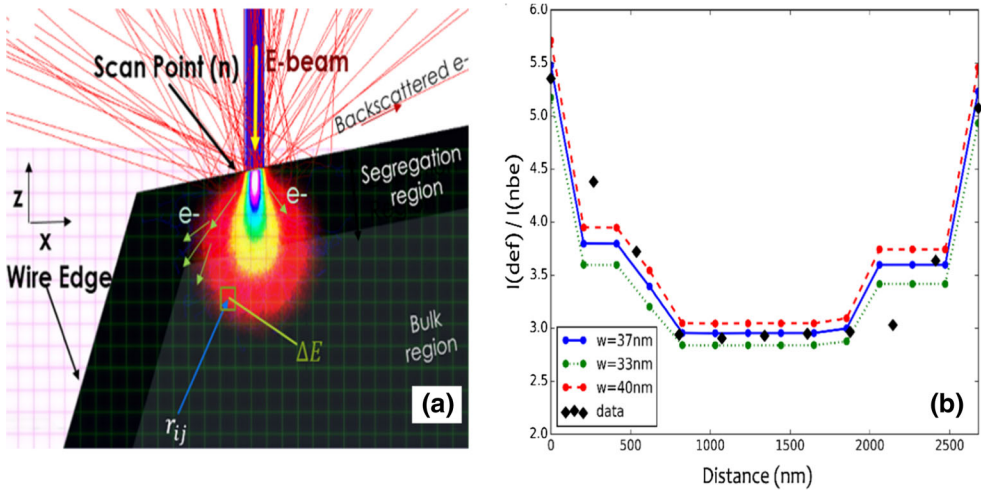

Fig. 2. (a) Schematic illustration of DRCLS line-scan measurement of defects in a PLD-grown hexagonal ZnO nanowire. (b) DRCLS line-scan plots of defect versus NBE intensities across a 2.2-μm-diameter nanowire showing best fit (blue line), error bounds (green and red lines), and measured data (black diamonds).[18] Permission granted by Royal Society of Chemistry.

are significant since they are electrically charged. Cu_{Zn} defects act as deep acceptors. V_O-related defects acts as donors. Degenerate n-type Ga doping induces V_{Zn} defects that compensate the electron doping. These electrically active defects will significantly impact charge transport at the nanoscale.

DRCLS measurement of defect nature, distribution, and density at the nanoscale enables new methods to control these defects and thereby the electric properties of nanostructures; For example, high-energy Ga-ion beams can implant Ga dopants to create ohmic contacts to ZnO.[20] Conversely, one can use low-energy Ga-ion beams to mill away the high-defect-density outer diameter of ZnO nanowires to produce Schottky-like or blocking contacts. Since these processes can be localized using focused beams, it is possible to create ohmic, Schottky, and blocking contacts all on the same nanowire using the same (Pt) metal.[21] Furthermore, because these electrically active defects are charged, one can apply external electrical fields to drive them across macroscopic distances. Figure 3 shows how V_{Zn} and Cu_{Zn} defects can be driven across the depletion region of ZnO by applied fields of tens of kV.[22] Here, a positive voltage attracts negatively charged acceptors over distances exceeding 100 nm. Incident electron beams directed through the metal contact provide depth profiles that show how such fields move defects toward the anode. Analogous electric-field-driven defect movement is observed laterally between electrodes on a ZnO surface.[23] Overall, the ability to control the type, density, and spatial arrangement of these defects provides a new avenue to creating nanoscale wide-bandgap semiconductor nanodevices.

Defect characterization and imaging of wide-bandgap semiconductors extend to state-of-the-art devices. Depth- and laterally resolved CLS provides information about temperature, lattice strain, defects, and atomic composition in high-power,

high-frequency transistors. Figure 4a illustrates the three-dimensional layer structure of an AlGaN/GaN high-electron-mobility transistor (HEMT), with arrows indicating the spatial range of DRCLS excitation both laterally and in depth. Of particular importance is the 2DEG layer (shown in red), the channel in which conduction takes place. Normal HEMT operation generates heat and mechanical strain due to the high voltages and currents involved. To measure local temperatures, one can monitor the NBE energy, which decreases with increasing temperature. The averaged dependence of energy versus temperature measured experimentally has a linear slope of $-5.98 \pm 0.12 \times 10^{-4}$ eV/°C for GaN.[24] Figure 4b shows a contour map of temperature measured on a line between gate and drain and extending from the surface past the 2DEG layer into the GaN layers.[25] Also displayed are the energies corresponding to depths of peak e-h excitation depth U_0 obtained from a Monte Carlo simulation[26] through the Si_3N_4 passivation surface layer of this HEMT structure. As shown, the hottest spot in this effective cross-sectional map under ON conditions is at the drain-side gate edge, in agreement with device modeling simulations.[27,28]

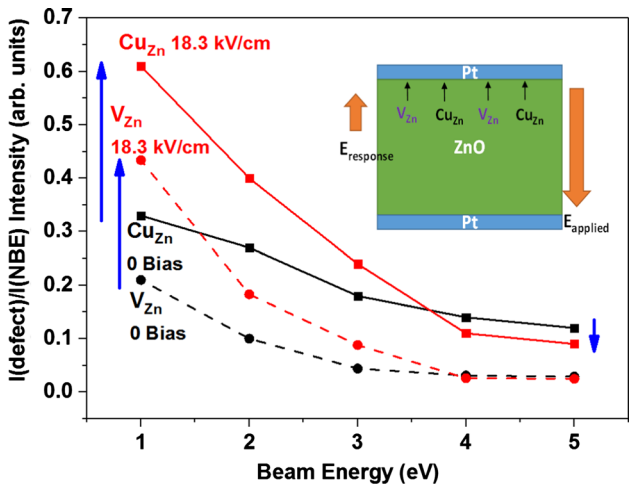

Fig. 3. DRCLS intensity ratio of V_{Zn} and Cu_{Zn} peaks in ZnO versus NBE intensity with and without an 18.3 kV/cm positive bias applied across a 0.5-mm ZnO crystal.[22] Reprinted with AIP permission.

Spatially localized measurements of mechanical strain are also useful to understand HEMT failure during operation. A key indicator of device degradation is current leakage between gate and drain I_{DG} with negative bias gate voltage. These OFF conditions induce mechanical strain between gate and 2DEG channel that is highest at the drain-side gate foot. As with temperature, strain also produces NBE shifts, here shifting to higher energy by 26 meV/GPa.[29,30] With increasing drain-gate voltage V_{DG}, I_{DG} rises sharply above a 28 V threshold voltage after an OFF-state, electric field-induced stress. At this voltage, the NBE shifts by 7 meV, corresponding to an increase in stress of 0.27 GPa. Added to the lattice-mismatch stress already induced in the AlGaN layer by the underlying GaN, this increase could exceed the mechanical strength of the crystal lattice due to an inverse piezoelectric effect.[31,32]

DRCLS coupled to Kelvin probe force microscopy (KPFM) measurements of electric potential across surfaces provides imaging correlations between native point defects measured optically and electronically. KPFM measures electric potential differences between a scanning atomic force microscopy (AFM) tip and the bare AlGaN HEMT surface, providing two-dimensional maps of surface work function after device operation. KPFM maps of source-gate-drain regions with increasingly negative V_{DG} (OFF conditions) reveals the appearance of low-potential regions at similar threshold voltages, regions that expand with increasing applied stress. Indeed, transistor failure occurs at regions with the most negative potential areas. Figure 5a illustrates an SEM secondary-electron image of a drain-gate-source region with a crater at the transistor's failure

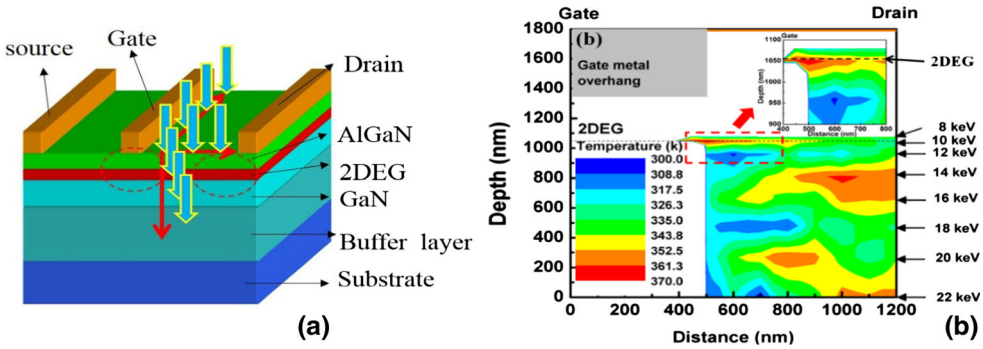

Fig. 4. (a) Three-dimensional layer structure of AlGaN/GaN HEMT. Arrows show lateral and depth positions of DRCLS excitation. (b) Contour maps of temperature in HEMT cross-section, showing elevated temperatures at drain-side gate edge and localized regions below. Inset shows expanded dashed region with 2DEG.[25] Reprinted with IEEE permission.

point.[33] Figure 5b illustrates the corresponding KPFM potential maps of the extrinsic drain and source regions to either side of a CL map of NBE emission intensity. Dashed circles indicate increased potential regions that align with regions of lower NBE emission. In turn, CL spectra of these regions display increased characteristic 2.3-eV "yellow band" (YB) and 2.8-eV "blue band" (BB) defect emission.[34,35] Indeed, surface potential exhibits a linear dependence on NBE-normalized YB and BB intensities, decreasing as defect emission intensities increase. Hence, both surface potential and CL measurements can map the defects. This correlation is consistent with increased acceptor densities in the AlGaN layer introducing a negative dipole that lowers the measured surface E_F.[24]

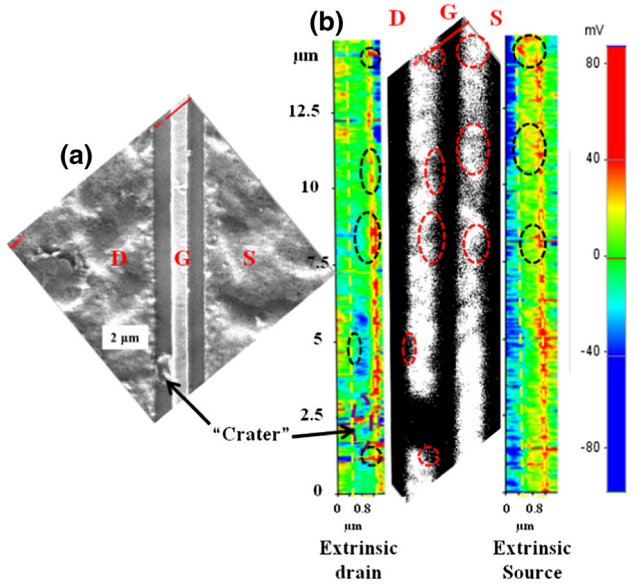

Fig. 5. (a) SEM secondary-electron image of AlGaN/GaN HEMT gate region showing crater formed after device failure. (b) CL map of NBE emission (middle) and KPFM map of potential (side). Dashed lines delineate extrinsic drain and source areas. Both red and black circles show similar higher defect and higher potential regions for CL and KPFM maps.[33] Reprinted with AIP permission.

The energies of all these features are in good agreement with GaN defect energies measured by deep-level optical spectroscopy (DLOS)[36–44] showing a dominant DLOS trap at E_C—0.55 eV with trap density of 10^{12} cm^{-2}. The bandgap complement of this energy level at 2.85 eV is consistent with the 2.8-eV BB emission. Likewise, the bandgap complement of a 1.1-eV DLOS-measured trap is 2.3 eV, in agreement with the 2.3-eV luminescence. DRCL spectra exhibit additional peak features corresponding to AlGaN defects and their NBE. SPS complements CLS measurements by identifying the position of the deep-level defects in the semiconductor bandgap with respect to the band edges. Onsets of photostimulated carrier population or depopulation result in potential changes that identify respectively the valence band (E_V) or conduction band (E_C) nature of the optical transition. SPS of the AlGaN surface yields energy thresholds corresponding to AlGaN trap levels of E_C—0.6 eV, 1.35 eV, 1.7 eV, and 2.0 eV, all in agreement with DLOS results. DRCL spectra as a function of depth for the E_C—2.0 eV YB peak, the E_C—1.35 eV BB peak, and a 3.75-eV feature (E_C—0.6 eV bandgap complement) map defect distributions below the HEMT surface. Figure 6 illustrates the measurement of these NBE-normalized peak intensities from the dashed region indicated in the HEMT layer diagram. These depth profiles show that YB densities decrease steadily from the outermost $Al_xGa_{1-x}N$ surface passivation layer, through the 50-nm AlGaN strain layer, and into the GaN substrate. In contrast, both the BB and the 3.75-eV defects exhibit peak intensities inside the AlGaN layer. Thus, DRCLS depth profiles are able to map out the various depth dependences of HEMT defects on a scale of tens of nanometers or less and identify specific defects with specific layers.

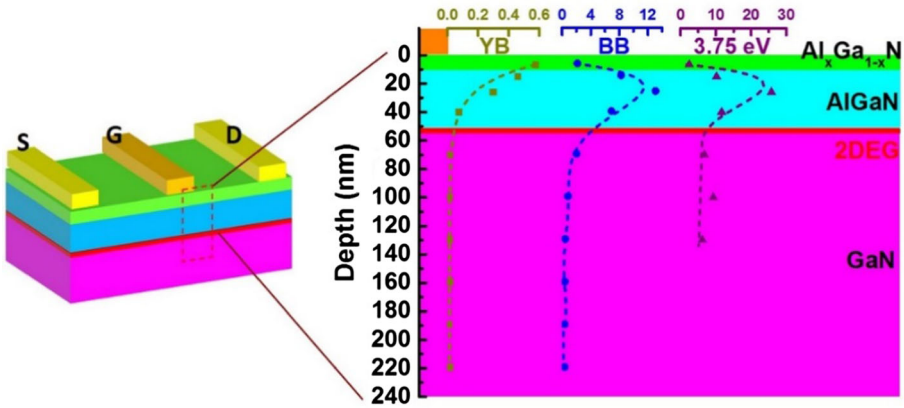

Fig. 6. AlGaN/GaN HEMT structure with dashed rectangle indicating region near the drain-side gate edge where yellow band (YB), blue band (BB), and 3.75-eV AlGaN deep-level defect densities are measured versus depth.

CONCLUSIONS

The results presented herein show that spatially resolved DRCLS can characterize, image, and in some cases, enable control of native point defects at wide-bandgap semiconductor interfaces and nanostructures in three dimensions and on a nanometer scale. CLS hyperspectral imaging reveals native point defects inside wide-bandgap nano- and microwires. The physical nature and spatial distribution of these defects can vary strongly with their method of growth. DRCLS can also measure the movement of defects under applied electric fields and their reduction by removing material in which DRCLS measures their segregation. Three-dimensional mapping of wide-bandgap devices can measure temperature and stress at localized regions that contribute to device degradation and failure. The ability to separate electric-field-induced strain effects from current-induced heating establishes their relative importance and underscores the importance of inverse piezoelectric effects for HEMT degradation. The capability to characterize and image defects can be extended to many other material systems, including 2D materials and interfaces, complex oxide heterojunctions, and nanoscale battery interfaces. Understanding the nature and distribution of defects in these systems may provide new avenues for their control.

ACKNOWLEDGEMENTS

L.J.B., G.M.F., W.T.R., J.C., and H.G. gratefully acknowledge National Science Foundation Grant No. DMR-1305195. L.J.B. acknowledges Office of Naval Research DRIFT MURI under Grant N00014-08-1-0655. H.v.W. and M.G. acknowledge Deutsche Forschungsgemeinschaft for support with Sonderforschungsbereich 762, "Functionality of oxide interfaces" and GR 1011/23-1.

REFERENCES

1. S.C. Dixon, D.O. Scanlon, C.J. Carmalt, and I.P. Parkin, *J. Mater. Chem. C* 4, 6946 (2016).
2. K. Ellmer, *Nat. Photonics* 6, 809 (2012).
3. H.Y. Hwang, Y. Iwasa, M. Kawasaki, B. Keimer, N. Nagaosa, and Y. Tokura, *Nat. Mater.* 11, 103 (2012).
4. D.P. Kumah, A.S. Disa, J.H. Ngai, H. Chen, A. Malashevich, J.W. Reiner, S. Ismail-Beigi, F.J. Walker, and C.H. Ahn, *Adv. Mater.* 26, 1936 (2014).
5. R.S. Pengelly, S.M. Wood, J.W. Milligan, S.T. Sheppard, and W.L. Pribble, *IEEE Trans. Microw. Theory Technol.* 60, 1764 (2012).
6. G. Meneghesso, G. Verzellesi, F. Danesin, F. Rampazzo, F. Zanon, A. Tazzoli, M. Meneghini, and E. Zanoni, *IEEE Trans. Dev. Mater. Reliab.* 8, 332 (2008).
7. L.J. Brillson, *J. Phys. D Appl. Phys.* 45, 183001 (2012).
8. L. Kronik and Y. Shapira, *Surf. Sci. Rep.* 37, 1 (1999).
9. A. Rose, *RCA Rev.* 27, 600 (1966).
10. B.G. Yacobi and D.B. Holt, *Cathodoluminescence Microscopy of Inorganic Solids* (New York: Plenum, 1990).
11. J. Christen, M. Grundmann, and D. Bimberg, *J. Vac. Sci. Technol. B* 9, 2358 (1991).
12. A. Gustafsson, M.-E. Pistol, L. Montelius, and L. Samuelson, *J. Appl. Phys.* 84, 1715 (1998).
13. K. Thonke, I. Tischer, M. Hocker, M. Schirra, K. Fujan, M. Wiedenmann, R. Schneidter, M. Frey, and M. Feneberg, *IOP Conf. Ser.: Mater. Sci. Eng.* 55, 012018 (2014).
14. H.L. Mosbacker, S. El Hage, M. Gonzalez, S.A. Ringel, M. Hetzer, D.C. Look, G. Cantwell, J. Zhang, J.J. Song, and L.J. Brillson, *J. Vac. Sci. Technol. B* 25, 1405 (2007).
15. L.J. Brillson, H.L. Mosbacker, M.J. Hetzer, Y. Strzhemechny, G.H. Jessen, D.C. Look, G. Cantwell, J. Zhang, and J.J. Song, *Appl. Phys. Lett.* 90, 102116 (2007).
16. S. Tumakha, D.J. Ewing, L.M. Porter, Q. Wahab, X. Ma, T.S. Sudharshan, and L.J. Brillson, *Appl. Phys. Lett.* 87, 242106 (2005).
17. D.J. Ewing, L.M. Porter, Q. Wahab, X. Ma, T.S. Sudharshan, S. Tumakha, M. Gao, and L.J. Brillson, *J. Appl. Phys.* 101, 114514 (2007).
18. W.T. Ruane, K.M. Johansen, K.D. Leedy, D.C. Look, H. von Wenckstern, M. Grundmann, G.C. Farlow, and L.J. Brillson, *Nanoscale* 8, 7631 (2016).
19. L.J. Brillson, W.T. Ruane, H. Gao, Y. Zhang, J. Luo, H. von Wenckstern, and M. Grundmann, *Mater. Sci. Semicond. Process.* 57, 197 (2017).
20. J. He, J. Ke, P. Chang, K. Tsai, P. Yang, and I. Chan, *Nanoscale* 4, 3399 (2012).
21. A. Jarjour, J.W. Cox, W.T. Ruane, H. Von Wenckstern, M. Grundmann, and L.J. Brillson, *Ann. der Physik*, 530, 1700335 (2018).
22. G.M. Foster, H. Gao, G. Mackessy, A.M. Hyland, M.W. Allen, B. Wang, D.C. Look, and L.J. Brillson, *Appl. Phys. Lett.* 111, 101604 (2017).
23. H. Gao, G.M. Foster, A.M. Hyland, M.W. Allen, and L.J. Brillson, unpublished.
24. A.P. Young and L.J. Brillson, *Appl. Phys. Lett.* 77, 699 (2000).
25. C.-H. Lin, T.A. Merz, D.R. Doutt, J. Joh, J.A. del Alamo, U.K. Mishra, and L.J. Brillson, *IEEE Trans. Electron Devices* 59, 2667 (2012).
26. D. Drouin, A. Réal Couture, D. Joly, X. Tastet, V. Aimez, and R. Gauvin, *Scanning* 29, 92 (2007).
27. W.D. Hu, X.S. Chen, Z.J. Quan, C.S. Xia, W. Lu, and P.D. Ye, *J. Appl. Phys.* 100, 074501 (2006).
28. I. Ahmad, V. Kasisomayajula, M. Holtz, J.M. Berg, S.R. Kurtz, C.P. Tigges, A.A. Allerman, and A.G. Baca, *Appl. Phys. Lett.* 86, 173503 (2005).
29. C.H. Lin, D.R. Doutt, U.K. Mishra, T.A. Merz, and L.J. Brillson, *Appl. Phys. Lett.* 97, 223502 (2010).
30. K. Wan, A. Alan Porporati, G. Geng, H. Yang, and G. Pezzotti, *Appl. Phys. Lett.* 88, 251910 (2006).
31. J.A. del Alamo and J. Joh, *Microelectron. Reliab.* 49, 1200 (2009).
32. J. Joh and J.A. del Alamo, *Microelectron. Reliab.* 50, 767 (2010).
33. C.-H. Lin, T.A. Merz, D.R. Doutt, M.J. Hetzer, J. Joh, J.A. del Alamo, U.K. Mishra, and L.J. Brillson, *Appl. Phys. Lett.* 95, 033510 (2009).
34. U. Kaufmann, M. Kunzer, H. Obloh, M. Maier, Ch. Manz, A. Ramakrishnan, and B. Santic, *Phys. Rev. B* 59, 5561 (1999).
35. M.A. Reshchikov, D.O. Demchenko, A. Usikov, H. Helava, and Yu. Makarov, *Phys. Rev. B* 90, 235203 (2014).
36. S. Kamiya, M. Iwami, T. Tsuchiya, M. Kurouchi, J. Kikawa, T. Yamada, A. Wakejima, H. Miyamoto, A. Suzuki, A. Hinoki, T. Araki, and Y. Nanishi, *Appl. Phys. Lett.* 90, 213511 (2007).
37. M. Arakawa, S. Kishimoto, and T. Mizutani, *Jpn. J. Appl. Phys. Part I* 36, 1826 (1997).
38. A.R. Arehart, A.C. Malonis, C. Poblenz, Y. Pei, J.S. Speck, U.K. Mishra, and S.A. Ringel, *Phys. Stat. Sol. C* 8, 2242 (2011).
39. A.R. Arehart, A.C. Malonis, C. Poblenz, Y. Pei, J.S. Speck, U.K. Mishra, and S.A. Ringel, *IEEE IEDM*, p. 20.1 (2010).

40. M. Ťapajna, U.K. Mishra, and M. Kuball, *Appl. Phys. Lett.* 97, 023503 (2010).
41. J. Joh and J.A. del Alamo, *IEEE Trans. Electron Devices* 58, 132 (2011).
42. M. Meneghini, A. Stocco, M. Bertin, D. Marcon, A. Chini, G. Meneghesso, and E. Zanoni, *Appl. Phys. Lett.* 100, 033505 (2012).
43. Y. Puzyrev, T. Roy, M. Beck, B.R. Tuttle, R.D. Schrimpf, D.M. Fleetwood, and S.T. Pantelides, *J. Appl. Phys.* 109, 034501 (2011).
44. D.W. Cardwell, A. Sasikumar, A.R. Arehart, S.W. Kaun, J. Lu, S. Keller, J.S. Speck, U.K. Mishra, S.A. Ringel, and J.P. Pelz, *Appl. Phys. Lett.* 100, 193507 (2012).